Supporting Information: Charge-Carrier Trapping Dynamics in Bismuth-Doped Thin Films of MAPbBr$_3$ Perovskite

Aleksander M. Ulatowski, Adam D. Wright, Bernard Wenger, Leonardo R.V. Buizza, Silvia G. Motti, Hannah J. Eggimann, Kimberley J. Savill, Juliane Borchert, Henry J. Snaith, Michael B. Johnston, and Laura M. Herz[*]

Department of Physics, University of Oxford, Clarendon Laboratory, Parks Road, Oxford OX1 3PU, United Kingdom

E-mail: laura.herz@physics.ox.ac.uk

Contents

1 Sample preparation

To obtain the precursor solutions, we prepared separately a $1.25\,\mathrm{M}$ MAPbBr$_3$ stock solution by dissolving $140\,\mathrm{mg}$ of MABr (Dyesol) and $459\,\mathrm{mg}$ of PbBr$_2$ (Alfa Aesar) per $1\,\mathrm{mL}$ of a solvent mixture of N'N-Dimethyl Formamide (DMF) and Dimethyl sulfoxide (DMSO) (in 4:1 volume ratio), and another stock solution of $1.25\,\mathrm{M}$ BiBr$_3$ (Sigma-Aldrich) in the same solvent (DMF/DMSO 4:1). The stock solutions were heated at 60°C for $15\,\mathrm{min}$ to accelerate the dissolution of the salts. The doped precursor solutions were made from the stock solutions with the following volumetric ratios: 0.1:99.9, 0.5:99.5, 1:99 and 5:95 (BiBr$_3$:MAPbBr$_3$,

1.25 M stock solutions). Despite the slightly decreasing concentration, the changes in thickness of the deposited films were negligible, according to their similar optical transmittance.

Thin films of MAPbBr$_3$ were deposited on z-cut quartz, 13 mm-diameter, 2 mm-thick disks. The substrates were cleaned in an ultrasonic bath with a sequence of soap (2% Hellmanex in deionised water), acetone and isopropanol, and finally treated under oxygen plasma for 10 min to remove organic residues. The solutions were spin-coated onto the substrates (1000 rpm for 10 s, then 6000 rpm for 35 s). A solvent-quenching step was then performed by quickly dropping 100 μL of anisole 10 s before the end of the spin-coating program. The films were then annealed at 100°C for 60 min on a hotplate and allowed to cool to room temperature.

2 Spectroscopic characterisation of optoelectronic properties

2.1 Absorption measurements

Thin-film absorption measurements were performed using a Bruker Vertex 80v FTIR spectrometer in both transmission and reflection geometry with a Si detector and a CaF$_2$ beamsplitter. A tungsten lamp was used as the light source. The absorption spectra of thin films were offset to 0 for below bandgap wavelengths. The initial non-zero absorption below the bandgap can be explained by scattering of light from the surface of the samples, which our measurement does not account for.

2.2 Elliott fitting

Elliott theory[1] describes the absorption of a semiconductor near the band edge. Here, we broadly follow the treatment described by Davies et al.,[2] in which the energy (E) dependent absorption, $\alpha(E, E_\text{g}, E_\text{b})$, is described by a combination of contributions from bound excitons

and electron-hole continuum states, involving the exciton binding energy E_b and band gap energy E_g:

$$\alpha(E, E_\mathrm{g}, E_\mathrm{b}) = \frac{b_0}{E} \sum_{n=1}^{\infty} \frac{4\pi E_\mathrm{b}^{3/2}}{n^3} \delta\left(E - \left[E_\mathrm{g} - \frac{E_\mathrm{b}}{n^2}\right]\right) + \frac{b_0}{E}\left[\frac{2\pi\sqrt{\frac{E_\mathrm{b}}{E-E_\mathrm{g}}}}{1 - \exp\left(-2\pi\sqrt{\frac{E_\mathrm{b}}{E-E_\mathrm{g}}}\right)}\right] c_0^{-1} \mathrm{JDoS}(E)$$

(S1)

where the joint density of states is given by $\mathrm{JDoS}(E) = c_0\sqrt{E - E_\mathrm{g}}$ for $E > E_\mathrm{g}$, and 0 otherwise, and the joint density of states constant $c_0 = \frac{1}{(2\pi)^2}\left(\frac{2\mu}{\hbar^2}\right)^{\frac{3}{2}} \times 2$, where μ is the reduced effective mass of the electron-hole system.

Broadening due to electron-phonon interactions, local fluctuations in the stoichiometry of the material, and energetic disorder is represented by convolution of $\alpha(E)$ with a normal distribution $N(0, \Gamma^2)$ which has mean 0 and standard deviation Γ. Unlike in the case of the modelling of absorption spectra of MAPbI$_3$ thin films reported recently,[2] we do not find a log-normal distribution to be additionally required to describe broadening in MAPbBr$_3$ perovskites.

The Elliott function, $f_\mathrm{Elliott} = \alpha(E, E_\mathrm{g}, E_\mathrm{b}) \otimes N(0, \Gamma^2)$, (where convolution is represented by the symbol $\otimes$) was fitted to the absorption onsets for the five samples by a least-squares minimisation method, with E_g fitted globally across all samples. The resultant Elliott fits are shown in Figure 1 in the main text and the extracted fit parameters are listed in Table 1 therein. We found that the experimental absorption data could be well described by a common band gap energy (E_g). E_b did not vary much between samples, whereas Γ increased with increasing bismuth doping.

2.3   Steady-state photoluminescence

Steady-state PL measurements were performed in reflection geometry. All PL curves shown in Figure 2 in the main text were spectrally corrected for the response of the detector using a tungsten calibration lamp of known spectrum. The lamp was placed in the sample position

and its spectrum was recorded by both Si and InGaAs detectors. The ratios of the measured lamp spectra to the reference spectrum provided by the manufacturer were used as spectral sensitivity curves for data correction. PL data shown in Figure S1 were left uncorrected.
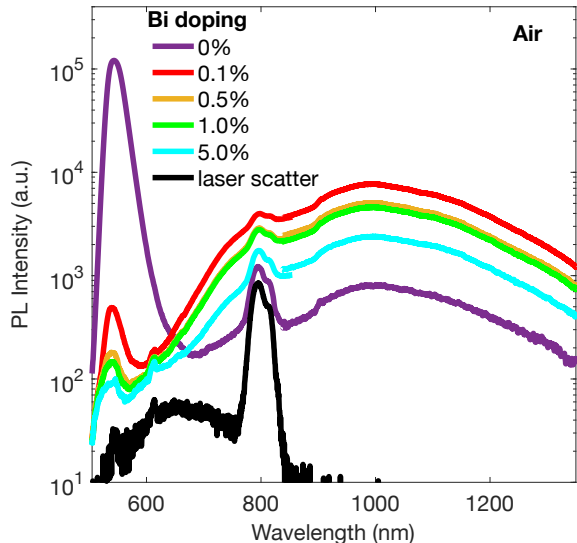

Figure S1: PL spectra of Bi-doped MAPbBr$_3$ thin films measured in air, shown on a logarithmic scale. The IR part of the spectrum, measured with InGaAs detector, was scaled to match the measurements of the Si CCD for the overlap region (800 nm-1000 nm).

The visible part of the spectrum shown in Figure 2 in the main text was measured using a TRIAX 190 spectrometer from HORIBA with a Si CCD detector (Symphony, HORIBA). The samples were excited in vacuum, using an ultrafast Ti-Sapphire laser (Mai Tai, Spectra Physics with 80 fs pulse width, 80 MHz repetition rate, frequency doubled to 400 nm). The IR region of the spectrum, shown in the same figure, was imaged using an InGaAs Symphony II detector from HORIBA and iHR320 spectrometer, with the samples excited in vacuum by a 405 nm diode laser with repetition rate of 80 MHz (LDH, PicoQuant).

Figure S1 shows the PL spectra measured in air with excitation at 470 nm (continuous wave LDH diode laser from PicoQuant). The spectra were measured using an iHR320 spectrometer from HORIBA with Si CCD and InGaAs detectors (Symphony II, HORIBA) for the visible and the IR range, respectively. The feature visible at 800 nm originated from scattered light from a Ti-Sapphire laser operating in the background at the time of the

measurement and does not originate from the samples. The spectrum plotted in black was measured with the 470 nm excitation laser turned off, showing the Ti-Sapphire scatter and a weak remaining background signal (at 700 nm) caused by room lights.

The spectra in Figure S1 were measured in air and differ from the ones presented in the main text in Figure 2, which were measured in vacuum. The main difference relates to the intensity of the emission from the undoped $MAPbBr_3$ sample, which is much stronger for the measurement in air. This effect was investigated previously by Motti et al.[3,4] and originates from trap passivation by molecular oxygen in the air, which reduces trap-mediated recombination pathways in the undoped films, allowing stronger band-edge emission as well as IR emission from the electron trapping defects. We note that the presence of oxygen does not have a strong effect on the emission from doped samples, which could indicate that the electron trapping mechanism, proposed in this letter to be the main source of trap-mediated recombination in Bi-doped $MAPbBr_3$ thin films, is not influenced by the presence of oxygen.

2.4   Time-resolved PL

Time-resolved photoluminescence (TRPL) was measured with a time-correlated single photon counting (TCSPC) setup. In this setup, the photoluminescence from the excited sample is directed through a monochromator (TRIAX 190, HORIBA) onto a Single-Photon Avalanche Diode (SPAD) detector (PDM, Micro Photon Devices). The detection of the decay transients at different wavelengths (band edge emission at 530 nm, IR emission at 900 nm and IRF at 410 nm) was performed by directing light of a chosen wavelength band onto the SPAD detector through use of the grating spectrometer. A separate 'gate' beam, originating from the same laser as the excitation beam, is used to trigger the SPAD detector. The detector measures the time delay between the triggering signal and an arrival of a photon from the sample. These arrival times are then plotted in the form of a histogram representing the decay of PL intensity as a function of time.

In order to measure the PL decay traces presented in Figure 3 in the main text, the

samples were excited at 400 nm with fluence of 40 nJ/cm^2, using an ultrafast Ti-Sapphire laser (Mai Tai, Spectra Physics - 80 fs pulse width, 80 MHz repetition rate, frequency doubled from 800 nm). The same laser was used to measure the Instrument Response Function (IRF) of the SPAD detector, which limits the resolution of the TCSPC setup. The IRF was measured by directing scattered light from the ultrafast laser onto the SPAD detector and recording the photon arrival histogram, which resulted in much slower decay (picoseconds FWHM) than expected for the laser pulse (80 fs FWHM). The IRF is shown in Figure S2 and was measured using 410 nm light derived by frequency doubling the tunable output of the laser.
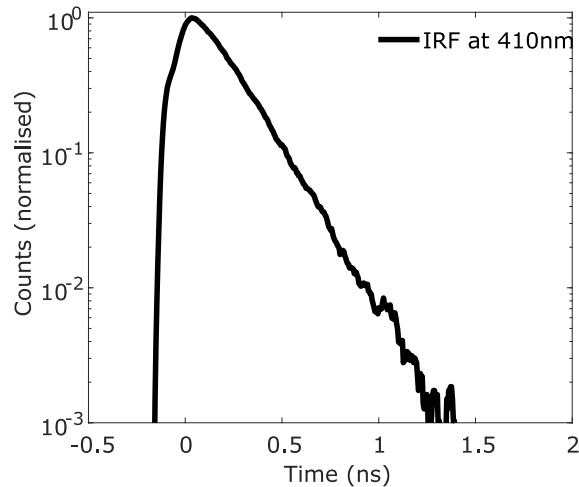

Figure S2: Instrument response function (IRF) of the TCSPC setup (for detection of 410 nm pulses) used to measure the time-resolved PL shown in Figure 3 in the main text. The decay time of the response is similar to the measured PL decay traces, implying that the actual PL decays may be shorter than measured.

3 THz Photoconductivity

The time-dependent photoconductivity measurement using an Optical-Pump–THz-Probe (OPTP) setup was described previously in multiple publications.[5–7] Briefly, the samples are photoexcited with pulses from an ultrafast (35 fs pulse) laser (800 nm Spectra Physics, Mai Tai - Ascend - Spitfire Ti-Sapphire regenerative amplifier, frequency doubled to 400 nm using a BBO crystal) operating at 5 kHz repetition rate. The fluence of the excitation is indicated in the figure legend for each measurement. After a time delay specified by the relative shift of optical delay stages, the sample is illuminated with THz radiation generated using a tri-layer spintronic emitter (2 nm tungsten, 1.8 nm $Co_{40}Fe_{40}B_{20}$, 2 nm platinum on quartz substrate)[8] and the transmitted THz radiation is measured using electro-optic sampling in a 0.2 mm (110)-ZnTe crystal with a 800 nm gate beam. The polarisation of the gate beam is then measured using a quarter-wave plate, polarising beam splitter and a balanced photodiode detector.

The pump beam is blocked every second THz pulse using an optical chopper and the transmitted THz radiation is compared for every two adjacent pulses (pump-on, pump-off). This approach provides the relative change of the THz transmission caused by the presence of photoexcited charge carriers. The photoconductivity σ of a thin film can be then expressed as:[5]

$$\sigma = -\frac{\epsilon_0 c}{d}(1 + n_{\text{substrate}})\frac{\Delta T}{T} \tag{S2}$$

where d is the thickness of the thin film, $n_{\text{substrate}}$ is the refractive index of the quartz substrate ($n_{\text{substrate}} = 2.13$), ΔT is the difference between the THz radiation transmitted through the illuminated sample and the sample in the dark, and T is the electric field strength of the THz radiation transmitted through the sample in the dark. ϵ_0 and c are the permittivity of free space and speed of light, respectively.

The mobility of the photoexcited charge carriers μ (which is the sum of electron and hole mobilities) can then be estimated from the onset of THz conductivity at time= 0, since from

the Drude model of conductivity (Equation 8 in the main text):

$$\sigma(t) = \mu_{\mathrm{e}} n(t) e + \mu_{\mathrm{h}} p(t) e \tag{S3}$$

where n and p are the number densities of photoexcited electrons and holes respectively, e is the electron charge and μ_{e} and μ_{h} are electron and hole mobilities, respectively. The initial number density of photoexcited charge carriers was estimated from the absorption spectra, under the assumption that all absorbed photons are converted to electron-hole pairs,[5] which is reasonable, given the low exciton binding energy in these materials.[9–11]

3.1   Modelling the photoconductivity decays

The model describing photoconductivity decays in this study was outlined in the main text. Briefly, the model takes into account the bimolecular (radiative) recombination of the photoexcited charge carriers, as well as the monomolecular (trap assisted) recombination with separate decay constants for electrons (k_1^{e}) and holes (k_1^{h}), and neglects the Auger (many-body) recombination pathway because of the relatively low pump fluences used in the study. By examining Figure S3 (which shows scaled photoconductivity decay traces for all bismuth doping concentration and three different excitation pump fluences) we can notice a strong dependence of the decay dynamics on the pump fluence only for the undoped film of MAPbBr$_3$. As explained in the main letter, this implies that we can neglect the bimolecular recombination pathway in all the doped samples, leading to a bi-exponential decay of photoconductivity (Equation 9 in the main text):

$$\sigma(t) = n_0 e [\mu_{\mathrm{e}} \exp\left(-k_1^{\mathrm{e}} t\right) + \mu_{\mathrm{h}} \exp\left(-k_1^{\mathrm{h}} t\right)] \tag{S4}$$

where n_0 is the initial number density of photoexcited electron-hole pairs, e is the charge of an electron and μ_{e} and μ_{h} are the charge-carrier mobilities of electrons and holes, respectively. We can also deduce from Figure S3 that the monomolecular decay rates of electrons and
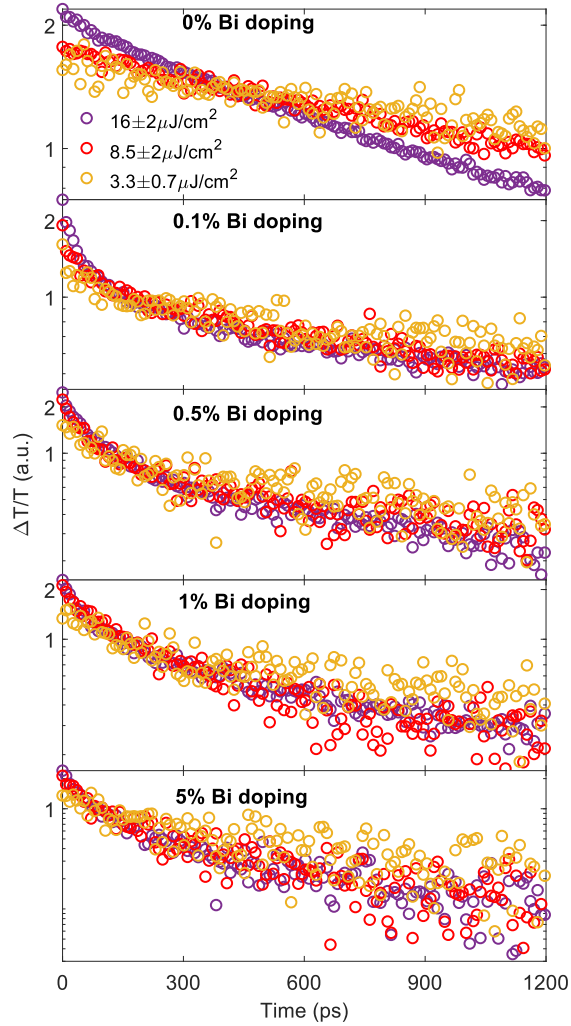
Figure S3: Photoconductivity decays in bismuth-doped MAPbBr$_3$ thin-films, shown on a logarithmic scale. The data were scaled using fits presented in Figure 4 in the main text as well as Figure S5, in order to avoid uncertainty caused by scaling the data to the first datapoint. The lowest measured pump fluence data were removed for clarity, as the relative noise for these decays was the largest. The excitation fluences are indicated by the legend.

holes are very similar in the case of the undoped (0% Bi doping) sample, since the low fluence photoconductivity decays monoexponentially (whereas for the doped samples we can observe a bi-exponential decay even for a low excitation fluence). This observation leads to the decay dynamics of photoexcited charge carriers being described by Equation 3 in the main text:

$$\frac{dn_{\mathrm{cc}}}{dt} = -k_1 n_{\mathrm{cc}} - k_2 n_{\mathrm{cc}}^2 \tag{S5}$$

where $n_{\mathrm{cc}} = n = p$ is the charge-carrier population density, equal for electrons (n) and holes (p), $k_1 = k_1^{\mathrm{e}} = k_1^{\mathrm{h}}$ is their monomolecular decay rate and k_2 is the radiative recombination constant. This results in an explicit solution of the form:

$$n_{\mathrm{cc}}(t) = \frac{k_1}{(k_2 + \frac{k_1}{n_0}) \exp(k_1 t) - k_2} \tag{S6}$$

where n_0 is the initial number density of photoexcited electron-hole pairs at $t = 0$.

Equations S4 and S6 were used to fit the THz photoconductivity data for the doped samples and undoped sample respectively using least-squares fitting method, as explained in details by Wehrenfennig et al.[5]

3.2   Determination of the ratio of electron to hole mobility

Due to the fast, selective trapping of electrons in bismuth-doped $MAPbBr_3$ thin films, the monomolecular decay constants of electrons and holes are significantly different, resulting in a bi-exponential decay of the photoconductivity (as seen in Equation S4 above). Since the electric conductivity is proportional to the number density and mobility of the charge carriers, the contribution of each exponential component to that bi-exponential decay is weighted by the mobility of electron and hole respectively. Hence, the ratio of the electron to hole mobility, $r = \frac{\mu_e}{\mu_h}$ has to be determined in order to fit the bi-exponential function to the photoconductivity decay traces.

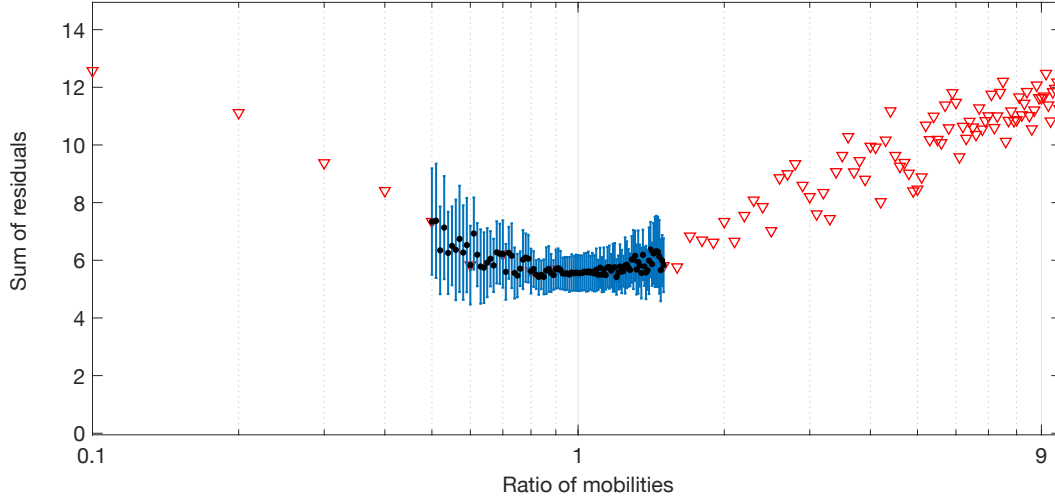In order to determine the ratio of the electron to hole mobility, we performed a compu-

Figure S4: Global optimisation of the fitting parameter 'r', representing the ratio of electron and hole mobilities, used in modelling photoconductivity decays. Two optimisation procedures have been used: coarse (red triangles) and fine (black dots) to find the optimal value of the parameter that minimises the sum of residuals for all fits to OPTP data for the doped samples. The value of $r = 1 \pm 0.2$ results in the lowest sum of residuals, therefore providing the best fit quality. The blue errorbars represent the standard deviation of the sums of residuals across all fits for the fine scan.

tational fitting procedure which stepped through the values of $r = \frac{\mu_e}{\mu_h}$ while fitting globally all the measured photoconductivity decay traces of the doped samples. For each value of r, the program calculates the sum of residuals of all the fits, representing the overall goodness of fits. This output has been plotted as a function of r in Figure S4. The value of $r = 1$ was used globally for all fits presented in this publication, as it results in the lowest sum of residuals.

The de-coupled behaviour of the electron and hole photoconductivity caused by selective electron trapping provides a unique insight into the mobility differences between the different charge carriers. These are usually obstructed by the similar decay rates of electrons and holes and only the total sum of mobilities can therefore typically be determined using OPTP measurements.

3.3 OPTP-full dataset

The photoconductivity decay traces for all samples are shown in Figure S5. Note that Figure 4 in the main text only showed a selected subset of these decays. Data for each doped sample were globally fitted for all excitation fluences with the bi-exponential decay function according to Equation 9 in the main text and the ratio of electron to hole mobilities $r = 1$ was used for all doped samples. The data for the undoped sample were fitted with a solution to Equation 3 in the main text, given by Equation S6. The samples were photoexcited by a 35 fs Ti-Sapphire laser (Spectra Physics, Mai Tai - Ascend - Spitfire Ti-Sapphire regenerative amplifier, frequency doubled) at 400 nm with fluences as indicated in the legends.
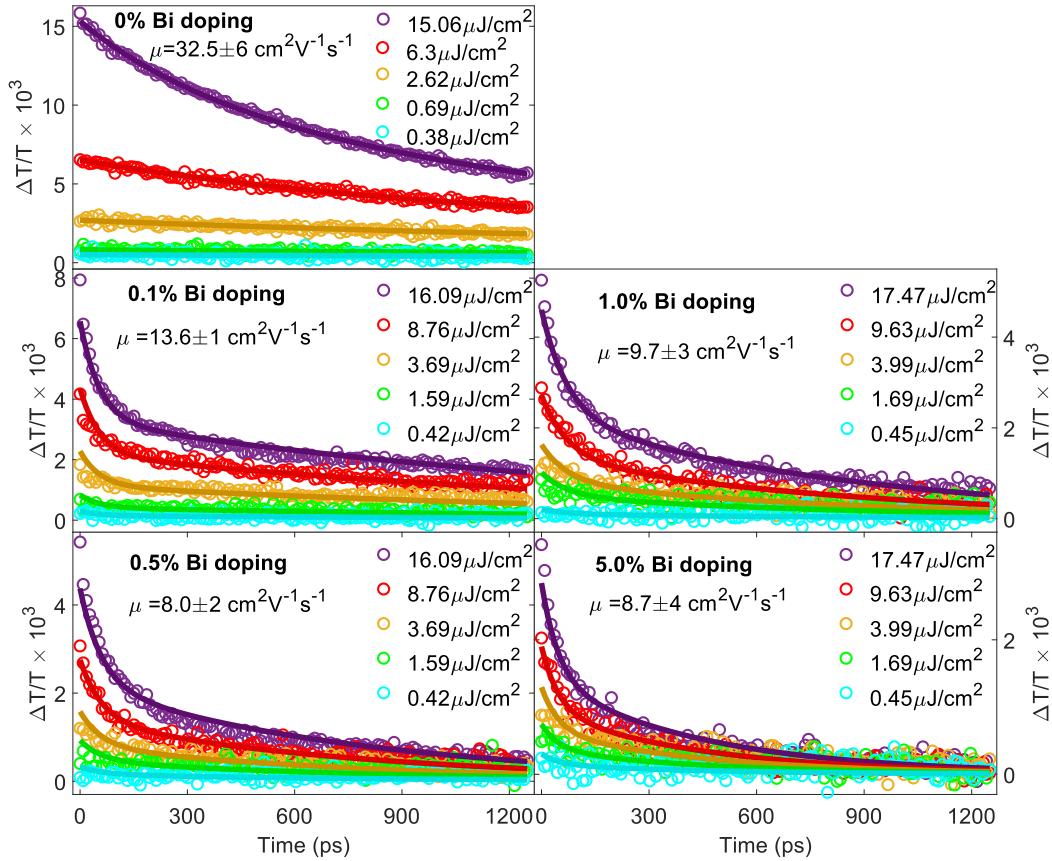
Figure S5: Photoconductivity decay traces for bismuth-doped thin films of MAPbBr$_3$ following excitation with a 35 fs duration, 400 nm wavelength laser pulse. The solid lines represent fit to the data (open circles) as explained in the main text. Excitation fluences are shown in the legends for each sample.

4   Structural characterisation

4.1   X-Ray Diffraction

The crystallinity of the thin films was characterised using an X-Ray Diffraction (XRD) measurement. A '$\theta : 2\theta$' scan was used with a copper K_α X-ray source. The diffraction patterns are shown in Figure S6. The spectra were corrected for tilt of the sample using the quartz substrate diffraction peak at $16.43°$ as a reference.[12]   Independently of the doping
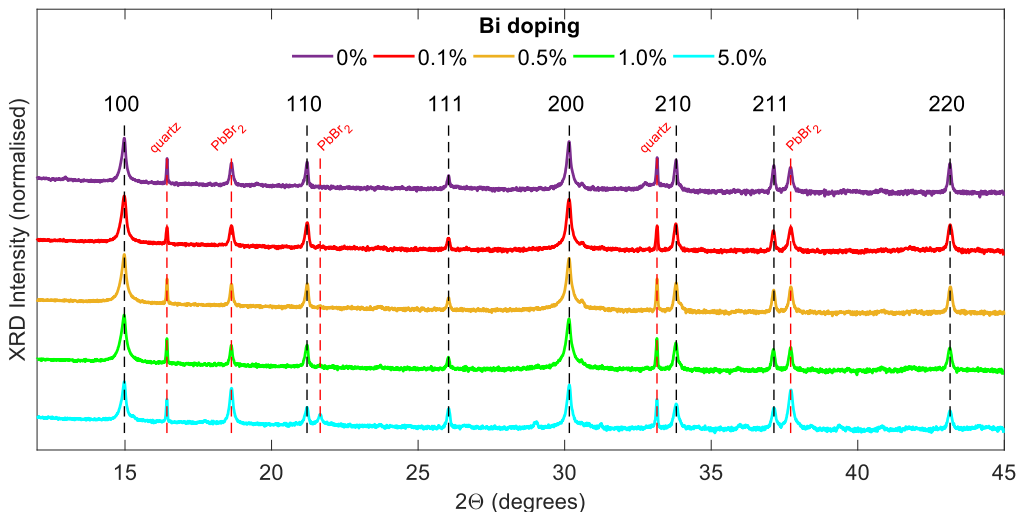

Figure S6: XRD spectra of bismuth-doped thin films of MAPbBr$_3$. The position of the peaks is unaffected by bismuth doping and closely resembles powder diffraction spectra of MAPbBr$_3$ reported by Wang et al.[13] Diffraction patterns are shown on a logarithmic scale and are offset from each other vertically for better visibility of the diffraction peaks.

level, all spectra show peaks at the diffraction angles that are consistent with previous reports of XRD spectra for MAPbBr$_3$.[13] To further investigate the effect of bismuth doping on the structure of the material, we compared both the intensity and broadening of the (100) diffraction peaks for different doping levels. From Figures S7 and S8 one can see that neither intensity nor broadening of the peak correlates with the doping level. We hence deduce that the presence of bismuth has a negligible effect on the crystallinity of these perovskite thin films, as larger crystallites would result in sharper diffraction peaks. We also note that the incorporation of bismuth into the perovskite crystals does not change the lattice parameter,
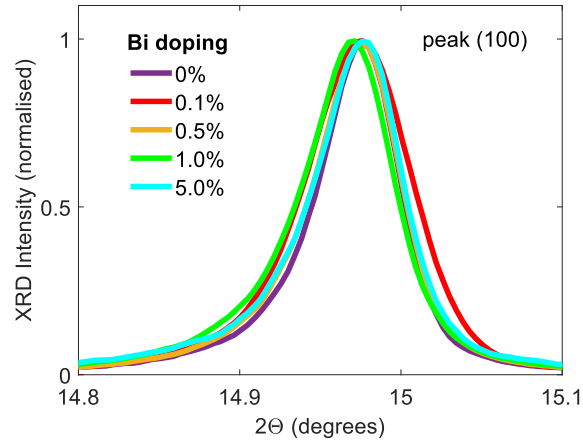
Figure S7: Normalised (100) X-ray diffraction peak, showing no correlation of peak broadening or position with bismuth doping level.
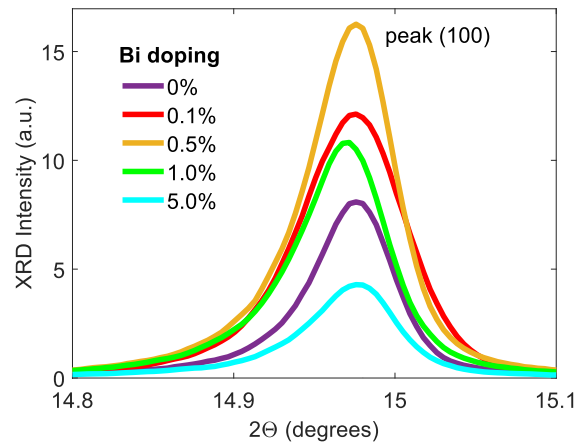

Figure S8: Unnormalised (raw) (100) X-ray difration peak, showing no correlation of intensity of the peak with doping level.

which would have caused shifts of the peak positions in the diffraction pattern. Therefore, in agreement with our observation that the bandgap is unaffected by doping, the presence of bismuth doping most likely leads to the introduction of point defects, either by enhancing the point defects already present in the MAPbBr$_3$ crystals[3] or by introducing new trapping energy states of very similar energetics to the halide interstitials.[14]

4.2 Phonon modes

In order to further examine the potential structural changes upon bismuth doping, we measured the THz transmission spectra of the perovskite thin films in the dark (no photoexcitation) to investigate the optical phonon modes of the lead-bromide lattice present in this spectral region, which had previously been observed by Zhao et al.[15] for undoped MAPbBr$_3$. Figure S9 shows the THz transmission spectra, presented as imaginary and real parts of the complex dark conductivity of the thin films. We find that bismuth doping has no effect on the spectral position and intensity of the peaks, therefore we conclude that it has no significant effects on the perovskite structure.
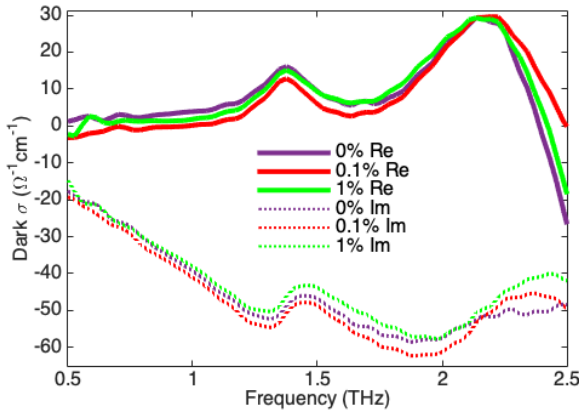

Figure S9: The position of the optical phonon modes of the lead-bromide lattice in MAPbBr$_3$ films, revealed by THz dark conductivity study show no changes when bismuth is added. This suggests bismuth doping does not result in significant changes to the crystal structure.

References

(1) Elliott, R. Intensity of optical absorption by excitons. *Physical Review* **1957**, *108*, 1384.

(2) Davies, C. L.; Filip, M. R.; Patel, J. B.; Crothers, T. W.; Verdi, C.; Wright, A. D.; Milot, R. L.; Giustino, F.; Johnston, M. B.; Herz, L. M. Bimolecular recombination in methylammonium lead triiodide perovskite is an inverse absorption process. *Nature Communications* **2018**, *9*, 293.

(3) Motti, S. G.; Meggiolaro, D.; Martani, S.; Sorrentino, R.; Barker, A. J.; De Angelis, F.; Petrozza, A. Defect Activity in Lead Halide Perovskites. *Advanced Materials* **2019**, *31*, 1901183.

(4) Motti, S. G.; Gandini, M.; Barker, A. J.; Ball, J. M.; Srimath Kandada, A. R.; Petrozza, A. Photoinduced emissive trap states in lead halide perovskite semiconductors. *ACS Energy Letters* **2016**, *1*, 726–730.

(5) Wehrenfennig, C.; Liu, M.; Snaith, H. J.; Johnston, M. B.; Herz, L. M. Charge-carrier dynamics in vapour-deposited films of the organolead halide perovskite $CH_3NH_3PbI_{3-x}Cl_x$. *Energy & Environmental Science* **2014**, *7*, 2269–2275.

(6) Tiwana, P.; Parkinson, P.; Johnston, M. B.; Snaith, H. J.; Herz, L. M. Ultrafast terahertz conductivity dynamics in mesoporous TiO_2: influence of dye sensitization and surface treatment in solid-state dye-sensitized solar cells. *The Journal of Physical Chemistry C* **2009**, *114*, 1365–1371.

(7) Wehrenfennig, C.; Eperon, G. E.; Johnston, M. B.; Snaith, H. J.; Herz, L. M. High charge carrier mobilities and lifetimes in organolead trihalide perovskites. *Advanced Materials* **2014**, *26*, 1584–1589.

(8) Seifert, T.; Jaiswal, S.; Martens, U.; Hannegan, J.; Braun, L.; Maldonado, P.;

Freimuth, F.; Kronenberg, A.; Henrizi, J.; Radu, I. et al. Efficient metallic spintronic emitters of ultrabroadband terahertz radiation. *Nature Photonics* **2016**, *10*, 483.

(9) Galkowski, K.; Mitioglu, A.; Miyata, A.; Plochocka, P.; Portugall, O.; Eperon, G. E.; Wang, J. T.-W.; Stergiopoulos, T.; Stranks, S. D.; Snaith, H. J. et al. Determination of the exciton binding energy and effective masses for methylammonium and formamidinium lead tri-halide perovskite semiconductors. *Energy & Environmental Science* **2016**, *9*, 962–970.

(10) Miyata, A.; Mitioglu, A.; Plochocka, P.; Portugall, O.; Wang, J. T.-W.; Stranks, S. D.; Snaith, H. J.; Nicholas, R. J. Direct measurement of the exciton binding energy and effective masses for charge carriers in organic–inorganic tri-halide perovskites. *Nature Physics* **2015**, *11*, 582.

(11) D'innocenzo, V.; Grancini, G.; Alcocer, M. J.; Kandada, A. R. S.; Stranks, S. D.; Lee, M. M.; Lanzani, G.; Snaith, H. J.; Petrozza, A. Excitons versus free charges in organo-lead tri-halide perovskites. *Nature Communications* **2014**, *5*, 3586.

(12) Patel, J. B.; Milot, R. L.; Wright, A. D.; Herz, L. M.; Johnston, M. B. Formation dynamics of $CH_3NH_3PbI_3$ perovskite following two-step layer deposition. *The Journal of Physical Chemistry Letters* **2015**, *7*, 96–102.

(13) Wang, K.-H.; Li, L.-C.; Shellaiah, M.; Sun, K. W. Structural and Photophysical Properties of Methylammonium Lead Tribromide ($MAPbBr_3$) Single Crystals. *Scientific Reports* **2017**, *7*, 13643.

(14) Li, J.-L.; Yang, J.; Wu, T.; Wei, S.-H. Formation of DY center as n-type limiting defects in octahedral semiconductors: the case of Bi-doped hybrid halide perovskites. *Journal of Materials Chemistry C* **2019**, *7*, 4230–4234.

(15) Zhao, D.; Skelton, J. M.; Hu, H.; La-o Vorakiat, C.; Zhu, J.-X.; Marcus, R. A.; Michel-Beyerle, M.-E.; Lam, Y. M.; Walsh, A.; Chia, E. E. Low-frequency optical phonon

modes and carrier mobility in the halide perovskite $CH_3NH_3PbBr_3$ using terahertz time-domain spectroscopy. *Applied Physics Letters* **2017**, *111*, 201903.